How to cite: *Angew. Chem. Int. Ed.* **2023,** *62,* e202301681
International Edition: doi.org/10.1002/anie.202301681
German Edition: doi.org/10.1002/ange.202301681

VIP **K-S Batteries** *Very Important Paper*

Reducing Overpotential of Solid-State Sulfide Conversion in Potassium-Sulfur Batteries

*Chao Ye[+], Jieqiong Shan[+], Huan Li, Chun-Chuan Kao, Qinfen Gu, and Shi-Zhang Qiao**

Abstract: Improving kinetics of solid-state sulfide conversion in sulfur cathodes can enhance sulfur utilization of metal-sulfur batteries. However, fundamental understanding of the solid-state conversion remains to be achieved. Here, taking potassium-sulfur batteries as a model system, we for the first time report the reducing overpotential of solid-state sulfide conversion via the meta-stable S_3^{2-} intermediates on transition metal single-atom sulfur hosts. The catalytic sulfur host containing Cu single atoms demonstrates high capacities of 1595 and 1226 mAh g^{-1} at current densities of 335 and 1675 mA g^{-1}, respectively, with stable Coulombic efficiency of ≈100 %. Combined spectroscopic characterizations and theoretical computations reveal that the relatively weak Cu-S bonding results in low overpotential of solid-state sulfide conversion and high sulfur utilization. The elucidation of solid-state sulfide conversion mechanism can direct the exploration of highly efficient metal-sulfur batteries.

Introduction

Sulfur is a promising electrode material for next-generation energy storage devices because of its low cost and high-theoretical specific capacity of ≈1675 mAh g^{-1}. Sulfur electrodes can be conjugated with a range of metal anodes in rechargeable metal-sulfur (M-S) batteries and have demonstrated promising potential for practical energy-storage applications.[1–7] However, sulfur reduction reaction (SRR) and sulfur oxidation reaction (SOR) in M-S batteries involve conversions between various solid-state insulating elemental sulfur, metal disulfides and metal sulfides.[8,9] The high kinetical bottleneck of these solid-state sulfide conversions causes large overpotentials and incomplete conversion even under low rates, leading to low discharged capacity and fast capacity decay.[10–13] In addition, sluggish solid-state sulfide conversion results in aggravation and diffusion of the soluble polysulfides, causing severe "shuttle effect".[14] Recently, it is reported that solid-state and semi-solid-state conversion dominate the charge and discharge processes under lean electrolyte conditions, making it more challenging to fully realize the high energy density of the M-S batteries. For example, under a practical low electrolyte/sulfur ratio of 4 μL mg^{-1} in lithium-sulfur (Li-S) batteries, even soluble polysulfides tend to exist in semi-solid state. The sluggish conversion and resultant high overpotential were demonstrated as the main failure origin of Li-S batteries.[15] Therefore, catalysing solid-state sulfide conversion is a promising strategy to improve the sulfur utilization and energy density of the M-S batteries.[16]

Various catalysts such as homogeneous redox mediators (RMs) and heterogeous catalysts have been reported to boost solid-state conversion.[17–19] For example, Zhang and co-workers recently reported the combination of discharge RM cobaltocene and charge RM 1,4-naphthoquinone, the former mediates the liquid-solid conversion from the soluble polysulfides (LiPSs) to Li_2S, while the latter mediates the solid-liquid conversion from Li_2S to LiPSs and the liquid-solid conversion from LiPSs to S_8. The mixed-RM promotes the sulfur redox kinetics in both charge and discharge process.[20] Although various types of RMs can regulate sulfur redox kinetics, it has been realized that the overpotential of solid-state sulfide conversion is independent to the type of RMs but closely dependent on the surface properties of the solid-state sulfur species.[10] Therefore, the introduction of heterogeous catalytic sulfur host can effectively modify the surface properties and enhance charge transfer of the solid-state sulfur species, thus lowering the overpotential of the solid-state sulfide conversion.[16,21,22] However, due to the complexity of diverse sulfur-containing species, the elucidation of the solid-state sulfide conversion mechanism and identification of reaction pathways remain to be achieved in M-S batteries, which hinder the rational design of the highly efficient catalytic sulfur host materials.

Here we report the efficient catalysis of solid-state conversion between K_2S_3 and K_2S species (K_2S_3–K_2S) via a meta-stable S_3^{2-} intermediate mediated pathway on a range of transition metal single-atom sulfur hosts in potassium-sulfur (K-S) batteries, which is superior to the incomplete

[*] Dr. C. Ye,[+] Dr. J. Shan,[+] Dr. H. Li, C.-C. Kao, Prof. S.-Z. Qiao
School of Chemical Engineering and Advanced Materials, The University of Adelaide
Adelaide, SA 5005 (Australia)
E-mail: s.qiao@adelaide.edu.au
Dr. Q. Gu
Australian Synchrotron, ANSTO
800 Blackburn Rd., Clayton, VIC 3168 (Australia)
[+] These authors contributed equally to this work.

conversion on pristine nitrogen-doped carbon sulfur host (Scheme 1).

We track the humid-sensitive solid-state metal sulfides conversion and identify the dynamic evolution of S_3^{2-} intermediates during discharge and charge processes by employing in situ ultraviolet-visible (UV/Vis) spectroscop, in situ synchrotron X-ray diffraction (XRD) measurements and ex situ synchrotron X-ray absorption (XAS).[23–25] In-depth understanding can therefore be established for the reaction pathway and activity origin of the solid-state sulfide conversion in K-S batteries.[26,27] More importantly, we applied cluster models to represent solid-state metal sulfides, which allows more accurate and efficient investigations on catalytic behavior compared with using the conventional molecular models.[28] The combination of in situ spectroscopic characterizations and density functional theory (DFT) computations successfully reveals the activity origin of the solid-state sulfide conversion, which is closely dependent on the atomic structure of sulfur host. As a result, on a sulfur electrode made from Cu single-atom catalytic sulfur host, we achieved high capacities of 1595 and 1226 mAh g^{-1} at specific currents of 335 and 1675 mA g^{-1}, respectively, together with stable Coulombic efficiency of ≈100 % during cycling. The superior electrochemical performance of Cu single-atom sulfur host can be attributed to the reduced overpotential of the K_2S_3–K_2S solid-state conversion originated from relative weak Cu-S bonding during sulfur redox processes. Therefore, we for the first time elucidate the reaction pathway of K_2S_3–K_2S solid-state conversion in K-S batteries, which can direct the rational design of sulfur electrodes with high sulfur utilization towards efficient M-S batteries.

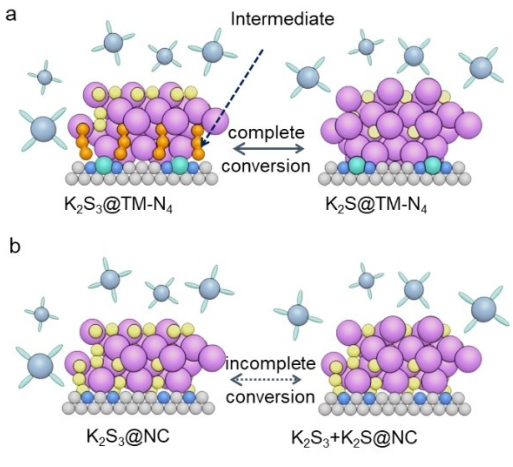

Scheme 1. Schematics of the solid-state sulfide conversion on a) transition metal single-atom materials and b) nitrogen-doped carbon (NC), in which the purple, yellow, grey, blue, orange, and light blue spheres represent K, S, C, N, transition metal single atoms and solvated K^+, respectively.

Results and Discussion

K_2S_3–K_2S solid-state conversion in K-S batteries

We prepared a series of sulfur hosts of transition metal single atoms decorated N-doped carbon (TM-N_4, TM = Mn, Fe, Co, Ni, Cu) via a general synthesis strategy of pyrolyzing heterometal-incorporated zeolite imidazole frameworks.[29] As evidenced by scanning electron microscopy (SEM) images (Figure S1–S4), various TM-N_4 and N-doped carbon (NC) sulfur hosts demonstrate similar transition metal mass fraction, size and cubic morphology, which allows comparable sulfur mass fractions in the active sulfur materials determined by thermogravimetric analysis (TGA, Figure S5) and the resultant sulfur electrodes (S/TM-N_4 and S/NC). To investigate the conversion of sulfur species during charge/discharge processes, we performed ex situ S K-edge X-ray absorption near edge structure (XANES) analysis on sulfur electrodes tested at different states of charge/discharge. Initially, the sulfur electrodes show a feature at 2472.5 eV at open circuit voltage (OCV), corresponding to the S 1s to π* electron transition of elemental sulfur (Figure 1a and b).[30] Taking S/Cu-N_4 as an example, the peak at 2472.5 eV gradually shifts to a higher energy of 2473.0 eV with the electrode discharging from 1.5 to 0.5 V. An additional peak at 2477.0 eV can be observed since discharged to 1.0 V. Both features can be assigned to S^{2-}, indicating the transformation from elemental S to K_2S.[31] During the following charge process, the peak at 2473.0 eV shifts back to 2472.5 eV in the potential range of 2.0–2.5 V, while the peak

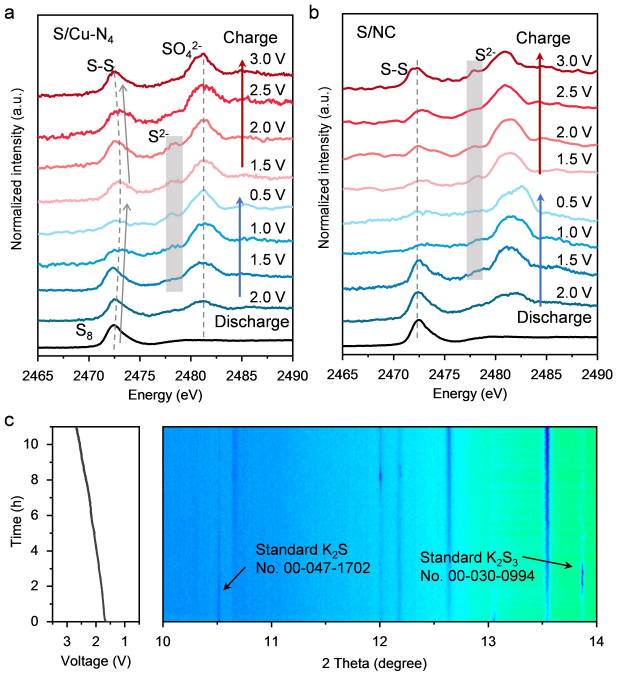

Figure 1. K_2S_3–K_2S solid-state conversion in K-S batteries. Ex situ NEXAFS of S K-edge of a) S/Cu-N_4 and b) S/NC in various discharge and charge states. c) Galvanostatic charge curve and corresponding in situ synchrotron XRD patterns for S/Cu-N_4 electrode.

at the 2477.0 eV disappears after charged to 2.0 V, suggesting that K_2S can be fully oxidized into sulfur during charging process. In contrast, for the S/NC and S/Mn-N_4 electrodes, both features associated with K_2S remain at the end of charge process, demonstrating the incomplete oxidation of K_2S (Figure 1b and Figure S6). This reveals the improved sulfur utilization of S/Cu-N_4 in comparison with other electrodes.

To further identify the solid-state sulfur species and elucidate the solid-state sulfide conversion in the K-S batteries, we conducted in situ synchrotron XRD measurements on S/Cu-N_4 in transmission mode using an in-house design 2032-type coin-cell.[24] As is shown in Figure 1c, during charge process starting from 1.7 V, a peak emerges at 10.5° and is assigned to the (2 0 0) facet of K_2S (No. 00-047-1702). Further charge from 1.7 to 2.0 V results in the emergence of another peak at 13.9° that is corresponding to the (−2 1 2) facet of solid-state insoluble K_2S_3 (No. 00-030-0994), and disappears after 2.0 V. Subsequently, three peaks at 12.2°, 10.7° and 12.6° become more evidence with increasing charge voltage to 2.7 V, which can be assigned to the (2 −2 2) facet of soluble K_2S_5 (No. 00-026-1336) and the (3 1 0) and (0 0 2) facets of soluble K_2S_6 (No. 04-021-7715), respectively. These results demonstrate the reversible conversion between K_2S_3 and K_2S of S/Cu-N_4 electrode, suggesting the favourable solid-state K_2S_3–K_2S conversion efficiency of Cu-N_4 catalytic sulfur host.

Meta-stable S_3^{2-} intermediates in solid-state conversion

To identify the intermediates and reaction pathway of the K_2S_3–K_2S solid-state conversion and investigate their behaviour on catalytic sulfur hosts, we employed in situ UV/Vis spectroscopy to monitor and differentiate possible intermediates of sulfur species, which has been widely applied in Li-S batteries.[32] Taking the Cu-N_4 sulfur host as an example, a wide peak at 280 nm corresponding to soluble long-chain polysulfides K_2S_x ($x=4$–8) can be observed during the discharge process from the potential of 0 to −1 V (vs. Ag/Ag^+), suggesting a liquid conversion process (Figure 2a). In the subsequent discharge process from −1.0 to −2.5 V, gradually decreased intensity of the peak at 280 nm is accompanied by the appearance of another peak at 260 nm, which can be identified as meta-stable S_3^{2-} species during the solid-state sulfide conversion.[32] This meta-stable S_3^{2-} species might be quickly disproportionated to S_4^{2-} and solid K_2S_3/K_2S species, making them difficult to be detected in ex situ characterizations. Similar phenomenon can be observed on the Mn-N_4 sulfur host, while the meta-stable S_3^{2-} species can hardly be detected on NC, demonstrating that the introduction of transition metal single atoms promotes the formation of the meta-stable S_3^{2-} species (Figure 2b and Figure S7). This result further supports the findings of in situ XRD and demonstrates that the introduction of TM-N_4 significantly affects the reaction pathway of solid-state conversion via generating polysulfide intermediates, which possibly leads to accelerated solid-state K_2S_3–K_2S conversion.

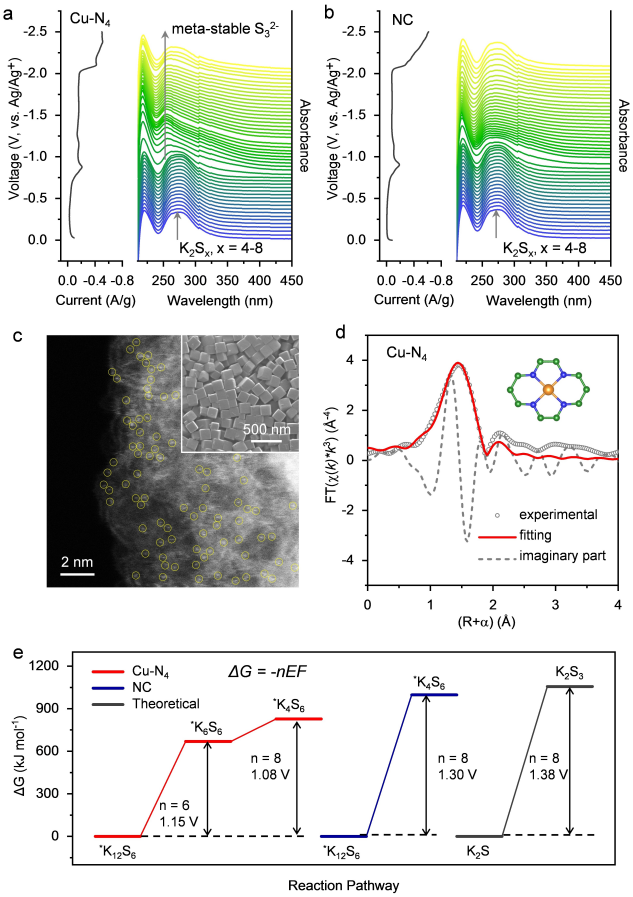

Figure 2. Meta-stable S_3^{2-} intermediates in the solid-state conversion. Galvanostatic discharge curve and corresponding in situ UV/Vis spectroscopy of the discharge process with a) Cu-N_4 and b) NC. c) HAADF-STEM image of Cu-N_4 in which Cu atoms are labelled as yellow-color circles. Inset is the representative SEM image of the Cu-N_4. d) Cu K-edge FT-EXAFS experimental spectra and the corresponding fitting of Cu-N_4. The dotted line represents the real parts of FT-EXAFS. Inset is the fitting model in which the green, blue, and orange spheres represent C, N and Cu atoms, respectively. e) Gibbs free energy profiles and reaction potential gaps according to the equation of $\Delta G=-nEF$ between solid K_2S, solid K_2S_3, $K_{12}S_6$ cluster, K_6S_6 cluster and K_4S_6 cluster.

We then analyzed the atomic structure and chemical properties of sulfur hosts to reveal the effect of intermediates. High-angle annular dark-field scanning transmission-electron microscopy (HAADF-STEM) image shows that the Cu single atoms, as labelled by yellow circles, are uniformly distributed in the carbon substrate (Figure 2c). Notably, the TM-N_4 sulfur hosts demonstrate similar atomic distribution of transition metal single-atom sites with comparable mass fractions of metal sites (Figure S8 and S9). More importantly, the Cu K-edge XANES spectrum of Cu-N_4 features a peak at 8987.8 eV due to 1s to 4p electron transition, which suggests higher valence states in comparison with standard Cu foil with a peak at 8979.1 eV (Figure S10). The Fourier transform (FT-) extended X-ray absorption fine structure (EXAFS) measurements were then performed to reveal the

local environment of transition metal sites.[33] The FT-EXAFS spectra and the corresponding fitting results demonstrate that the coordination number of Cu-N bonding is 4 with Cu–N distance of 1.94 Å, leading to postulation of dominant active sites as Cu-N_4 (Figure 2d).[33] Other TM-N distances are determined as 2.17, 2.02, 1.98, and 2.01 Å for Mn-N_4, Fe-N_4, C-N_4, and Ni-N_4, respectively (Figure S11–S14, Table S1). This allows rational determination of DFT structure models for TM-N_4 sulfur hosts.

DFT calculations were carried out using cluster models to investigate energetics of the solid-state K_2S_3–K_2S conversion.[28] Firstly, the standard potentials for the redox conversion between K_2S_3 and K_2S was calculated to be 1.38 V (vs. K^+/K) based on the Gibbs free energy changes (ΔG) of the corresponding formation reactions and the equation of $\Delta G = -nEF$. Subsequently, the NC, $K_{12}S_6$ and K_4S_6 clusters were employed as the substrate, reactant, and product, respectively (Figure S15). The resultant potential gap for the redox conversion between $K_{12}S_6$ and K_4S_6 clusters on the NC was calculated to be 1.30 V (vs. K^+/K), which is comparable to that of solid-state K_2S_3–K_2S conversion, validating the cluster models in simulating the solid-state sulfide conversion. For the Cu-N_4 catalyst, we proposed a two-step conversion mechanism: $K_{12}S_6 \rightarrow K_6S_6 + 6K^+ + 6e^-$ (step 1), $K_6S_6 \rightarrow K_4S_6 + 2K^+ + 2e^-$ (step 2), in which K_6S_6 was applied as the theoretical model of the meta-stable intermediate S_3^{2-} species (Figure S16). The free energy diagram for step 1 and step 2 on the Cu-N_4 surface was calculated with corresponding potentials of 1.15 and 1.08 V, respectively (Figure 2e). For the Mn-N_4, the overall overpotential of 1.13 V is lower than that of 1.30 V and 1.38 V (Figure S17 and S18). Therefore, the TM-N_4 catalytic sulfur host facilitates the two-step reaction pathway with the mediation of S_3^{2-} intermediates, which demonstrates lower energy gap of the solid-state K_2S_3–K_2S conversion than that of the NC sulfur host.

Electrochemical performance of S/TM-N_4 electrodes

It is expected that the favourable solid-state K_2S_3–K_2S conversion would result in enhanced electrochemical performance of the sulfur electrodes with various TM-N_4 sulfur hosts in K-S batteries. Accordingly, we conducted rating tests under varying current densities from 335 to 3350 mA g^{-1}. As is shown in Figure 3a, S/Cu-N_4 exhibits advantageous discharge capacities of 1633, 1062, 750 and 463 mAh g^{-1} under current densities of 335, 838, 1675 and 3350 mA g^{-1}, respectively. Among various sulfur electrodes, the rating capabilities decrease as ordered S/Cu-N_4 > S/Ni-N_4 > S/Co-N_4 > S/Fe-N_4 > S/Mn-N_4 (Figure S19). Additionally, a high capacity of 482 mAh g^{-1} can be delivered by S/Cu-N_4 following 30 continuous cycles under 838 mA g^{-1} with a stabilized CE held at around 100 %. In contrast, after rating and following cycling test, S/Ni-N_4, S/Co-N_4, S/Fe-N_4, S/Mn-N_4 and S/NC electrodes exhibit capacities of 372, 355, 317, 341, and 310 mAh g^{-1}, respectively.

We then evaluated cycling performance of various sulfur electrodes. Under 335 mA g^{-1}, S/Cu-N_4 delivers a high initial capacity of 1595 mAh g^{-1} and a decent capacity of 636 mAh g^{-1} after 50 cycles, which greatly outperforms the other sulfur electrodes (Figure 3b, S20 and S21). Significantly, the rate and cycling performances of S/Cu-N_4 are superior to most of the previously reported K-S cathodes (Table S2). In addition, under a large current density of 1675 mA g^{-1}, a high initial capacity of 1226 mAh g^{-1} and after-cycled capacity of 480 mAh g^{-1} after 100 continuous cycles are obtained on S/Cu-N_4 with a stabilized CE held at around 100 % (Figure 3c). For comparison, the S/Ni_4-N_4, S/Co-N_4, S/Fe-N_4, S/Mn-N_4 and S/NC exhibit much lower cycling capacities in comparison with that of S/Cu-N_4 (Figure S22). Therefore, it is demonstrated that benefited from the complete solid-state K_2S_3–K_2S conversion, S/Cu-N_4 exhibits the optimized sulfur utilization and high-capacity output among these S/TM-N_4 and S/NC sulfur electrodes.

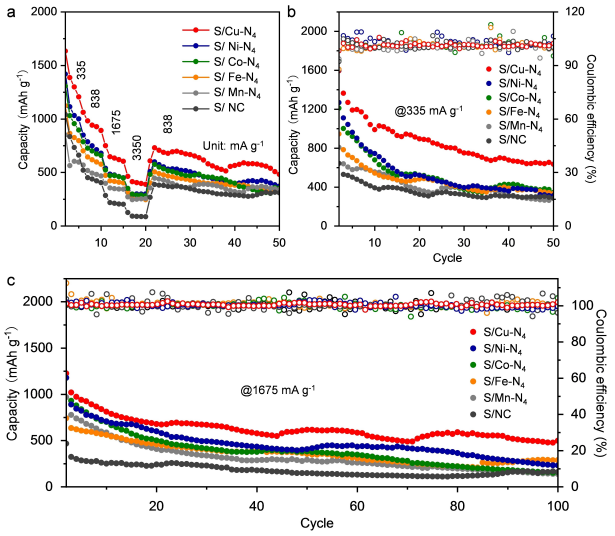

Figure 3. Electrochemical performance of S/TM-N_4 electrodes. a) Rate capabilities of sulfur electrodes of S/Cu-N_4, S/Ni-N_4, S/Co-N_4, S/Fe-N_4, S/Mn-N_4, S/NC for K-S batteries. Cycling performances and CE of various sulfur electrodes at current densities of b) 335 mA g^{-1} and c) 1675 mA g^{-1}.

Structure-property relationship of S/TM-N_4 electrodes

To elucidate the origin of the electrochemical performance of various S/TM-N_4 electrodes, we conducted ex situ XANES analysis of the discharged electrodes to investigate the interaction between transition metal and sulfur species. The Cu K-edge XANES spectrum of the discharged S/Cu-N_4 shows an additional weak pre-edge feature compared with that of pristine Cu-N_4, which can be attributed to the decreased symmetry of coordination environment of Cu sites as a result of bonding with S (Figure 4a). In addition, the discharged S/Cu-N_4 demonstrates a lower peak energy at 8984.5 eV in comparison with the pristine Cu-N_4, suggesting the decreased Cu valence state of the former. As shown in the inset of Figure 4a, the wavelet transform (WT)-EXAFS spectra display one region of intensity maximum at ca.

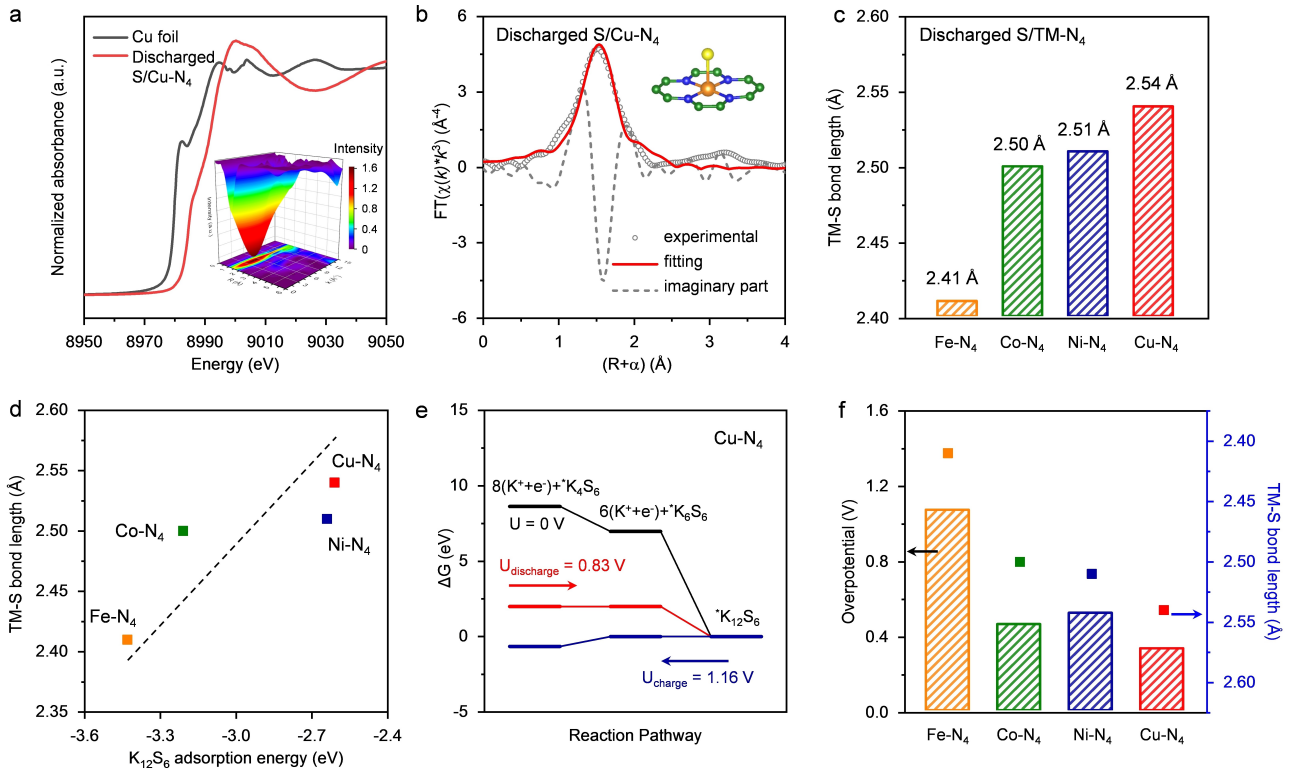

Figure 4. Electronic structure–property relationship of S/TM-N_4 electrodes. a) Cu K-edge XANES of the discharged S/Cu-N_4, the inset is the Cu K-edge WT-EXAFS. b) Cu K-edge FT-EXAFS experimental spectra and the corresponding fitting. The dotted line represents the real parts of FT-EXAFS. Inset is the fitting model in which the yellow, green, blue, and orange spheres represent S, C, N and Cu atoms, respectively. c) TM-S bond length determined by fitting of corresponding K-edge FT-EXAFS spectra of the TM-N_4. d) Linear relationship between TM-S bond length and K_2S adsorption energies on the TM-N_4. e) Gibbs free energy profiles and reaction potentials. f) Relationship between overpotentials (bars, left *y*-axis) and the K_2S adsorption energies (dots, right *y*-axis) on the TM-N_4.

4.5 $Å^{-1}$, suggesting the fully isolation of Cu single atoms with only first-shell coordination.[34,35] Further, the FT-EXAFS spectra and the corresponding fitting results demonstrate that the Cu-S bond exhibits a coordination number of 0.9 with a bond length of 2.54 Å (Figure 4b and S23). Similarly, the TM-S bond lengths of discharged S/Ni-N_4, S/Co-N_4, S/Fe-N_4 are determined to be 2.51, 2.50 and 2.41 Å, respectively (Figure 4c and S24–S26). It is therefore inferred that the bonding strength of the TM-S bond length follows the order of Cu-S < Ni-S < Co-S < Fe-S, which may reveal the origin of different sulfur utilization achieved on various S/TM-N_4 electrodes.

DFT calculations were then carried out with various TM-N_4 configurations including Mn, Fe, Co, Ni, Cu and Zn to establish the structure–property relationship on various S/TM-N_4 electrodes. Firstly, the adsorption energies of $K_{12}S_6$ on the TM-N_4 configurations were calculated to be −3.62, −2.61, −2.64, −3.21, −3.43, and −3.20 eV for Zn-N_4, Cu-N_4, Ni-N_4, Co-N_4, Fe-N_4, and Mn-N_4, respectively (Figure 4d and Figure S27–S30). This trend is consistent with that of the TM-S bond length as determined by FT-EXAFS analysis, suggesting that the Cu-N_4 exhibits relatively weak Cu-S bond with the discharge product K_2S in comparison with those of other TM-N_4. This trend indicates a linear relationship between the *d*-orbital filling of the TM sites and TM-S bonding strength. This can be explained by the crystal field theory: the bond strength of TM-S is determined by the occupation of the anti-bonding states σ* (hybridization of d_{z^2} orbital of TMs and p_z orbital of S) and π* (hybridization of $d_{xz/yz}$ orbital of TMs and $p_{x/y}$ orbital of S), which depends on the *d*-orbital electrons of the TM sites.[36] From Mn to Cu, their *d*-orbital electrons range from $3d^5$ to $3d^9$. For example, for the Mn-N_4, only π* states are slightly filled, resulting in strong Mn-S bonding. With the increasing occupation of 3*d* electrons to Cu, the π* and σ* states are gradually occupied, resulting in less effective in the *d*-*p* hybridization and weaker Cu-S bond. However, the Zn-N_4 exhibits stronger Zn-S bonding with the fully occupied *d* orbital electrons of $3d^{10}$. Furthermore, we calculated the free energy diagram with the proposed reaction mechanism to investigate the overpotential of the solid-state sulfide conversion reactions in K-S batteries. As shown in the Figure 4e, the starting free energy is set at zero potential at $K_{12}S_6$ cluster. For the step 1 from $K_{12}S_6$ to K_6S_6, Cu-N_4 exhibits a low free energy change (ΔG_{CuN4}-1) value of 6.98 eV, whilst the Zn-N_4, Ni-N_4, Co-N_4, Fe-N_4, and Mn-N_4 surfaces exhibit more positive values of 7.36, 7.32, 7.20, 8.34, and 8.13 eV, respectively. For the second step, Cu-N_4 shows the lowest free energy (ΔG_{CuN4}-2) value of 8.63 eV while Zn-N_4, Ni-N_4, Co-N_4, Fe-N_4, and Mn-N_4 surfaces exhibit more positive values of 9.02, 8.72, 8.68, 8.98, and 9.02 eV, respectively. More importantly, a linear relationship be-

tween ΔG_{TMN4}-1 and ΔG_{TMN4}-2 can be observed, indicating the positive correlation between the free energy of solid-state sulfide conversion and the *d*-orbital filling of TM sites (Figure S31). Next, the overpotentials are used to evaluate the performance of the solid-state conversions, calculated by $U_{charge} = (\Delta G_{TMN4}\text{-}1)/6e$ and $U_{discharge} = [(\Delta G_{TMN4}\text{-}2) - (\Delta G_{TMN4}\text{-}1)]/2e$. Taking the free energy diagram of Cu-N_4 as an example, during charge process, 1.16 V is the lowest potential where all the charging steps are downhill. During discharge process, 0.83 V is the highest potential where all the discharge steps are downhill. Therefore, the overpotential of solid-state sulfide conversion of Cu-N_4 can be determined as 0.33 V, representing the smallest overpotential and highest conversion activity among the TM-N_4 catalysts.[37] As shown in the Figure 4f, similar trends can be observed between the overpotentials and the TM-S bond length on various TM-N_4 (Figure S32). This demonstrates that the weaker TM-S bonding strength can result in smaller overpotential of the solid-state sulfide conversion, which provides fundamental insights for the rational design of efficient sulfur host.

Conclusion

In summary, we explored the catalysis of solid-state K_2S_3–K_2S conversion on a range of TM-N_4 single atom sulfur hosts to reveal the reaction mechanism and demonstrate pathway for achieving superior K-S battery performance. As evidenced by diverse in situ spectroscopic measurements including Synchrotron XRD and in situ UV/Vis, we for the first time identified the meta-stable S_3^{2-} intermediates and the corresponding solid-state K_2S_3–K_2S conversion pathway for K-S batteries. The designed Cu-N_4 sulfur hosts exhibit promoted meta-stable S_3^{2-} intermediates and accelerated solid-state K_2S_3–K_2S conversion kinetics. As a result, the S/Cu-N_4 sulfur electrode demonstrates remarkable initial discharge capacities of 1595 and 1226 mAh g^{-1} at specific current densities of 335 and 1675 mA g^{-1}, respectively, as well as high CE. Based on spectroscopic analysis and DFT calculations, a structure–property relationship on various S/TM-N_4 electrodes can be established. It is demonstrated that the *d*-orbital filling of the TM sites is closely related to the strength of TM-S bond with sulfur species during sulfur redox processes, which significantly affects the overpotentials of solid-state conversion reaction. The novel mechanism expands the current understanding of solid-state sulfide conversion chemistry in M-S batteries and will inspire future exploration of highly efficient electrode materials for advanced energy-related systems.

Acknowledgements

This work was financially supported by the Australian Research Council (FL170100154, DP220102596, IH200100035 and DE230101011). DFT computations were undertaken with the services from the National Computational Infrastructure (NCI) and Phoenix High Performance Computing supported by the Australian Government and The University of Adelaide. The authors thank Dr. Bruce Cowie and Dr. Bernt Johannessen at the ANSTO for the help in NEXAFS and XAS test. Part of the experiments was performed at Powder Diffraction and X-ray Absorption Spectroscopy beamlines at the Australian synchrotron, ANSTO. Open Access publishing facilitated by The University of Adelaide, as part of the Wiley - The University of Adelaide agreement via the Council of Australian University Librarians.

Conflict of Interest

The authors declare no conflict of interest.

Data Availability Statement

The data that support the findings of this study are available from the corresponding author upon reasonable request.

Keywords: Meta-Stable Intermediates · Metal-Sulfur Batteries · Single Atom Catalyst · Solid-State Conversion · Sulfur Host

[1] Y.-J. Lei, H.-L. Yang, Y. Liang, H.-W. Liu, B. Zhang, L. Wang, W.-H. Lai, Y.-X. Wang, H.-K. Liu, S.-X. Dou, *Adv. Energy Mater.* **2022**, *12*, 2202523.
[2] Y.-J. Lei, H.-W. Liu, Z. Yang, L.-F. Zhao, W.-H. Lai, M. Chen, H. Liu, S. Dou, Y.-X. Wang, *Adv. Funct. Mater.* **2023**, *33*, 2212600.
[3] H. Li, R. Meng, Y. Guo, B. Chen, Y. Jiao, C. Ye, Y. Long, A. Tadich, Q.-H. Yang, M. Jaroniec, S.-Z. Qiao, *Nat. Commun.* **2021**, *12*, 5714.
[4] Y. Wang, X. L. Huang, H. Liu, W. Qiu, C. Feng, C. Li, S. Zhang, H. K. Liu, S. X. Dou, Z. M. Wang, *ACS Nano* **2022**, *16*, 5103–5130.
[5] L. Zeng, J. Zhu, P. K. Chu, L. Huang, J. Wang, G. Zhou, X.-F. Yu, *Adv. Mater.* **2022**, *34*, 2204636.
[6] R. Zhu, W. Zheng, R. Yan, M. Wu, H. Zhou, C. He, X. Liu, C. Cheng, S. Li, C. Zhao, *Adv. Funct. Mater.* **2022**, *32*, 2207021.
[7] B.-W. Zhang, T. Sheng, Y.-X. Wang, S. Chou, K. Davey, S.-X. Dou, S.-Z. Qiao, *Angew. Chem. Int. Ed.* **2019**, *58*, 1484–1488.
[8] Y. Liu, X. Meng, Z. Wang, J. Qiu, *Sci. Adv.* **2022**, *8*, eabl8390.
[9] Y. Liu, X. Meng, Z. Wang, J. Qiu, *Nat. Commun.* **2022**, *13*, 4415.
[10] D. Cao, X. Shen, A. Wang, F. Yu, Y. Wu, S. Shi, S. A. Freunberger, Y. Chen, *Nat. Catal.* **2022**, *5*, 193–201.
[11] X. Chen, H. Ji, Z. Rao, L. Yuan, Y. Shen, H. Xu, Z. Li, Y. Huang, *Adv. Energy Mater.* **2022**, *12*, 2102774.
[12] Z. Hou, T. Zhang, X. Liu, Z. Xu, J. Liu, W. Zhou, Y. Qian, H. J. Fan, D. Chao, D. Zhao, *Sci. Adv.* **2022**, *8*, eabp8960.
[13] H. Li, R. Meng, Y. Guo, C. Ye, D. Kong, B. Johannessen, M. Jaroniec, S.-Z. Qiao, *Angew. Chem. Int. Ed.* **2022**, *61*, e202213863.
[14] L. Peng, Z. Wei, C. Wan, J. Li, Z. Chen, D. Zhu, D. Baumann, H. Liu, C. S. Allen, X. Xu, A. I. Kirkland, I. Shakir, Z. Almutairi, S. Tolbert, B. Dunn, Y. Huang, P. Sautet, X. Duan, *Nat. Catal.* **2020**, *3*, 762–770.
[15] G. Ye, M. Zhao, L.-P. Hou, W.-J. Chen, X.-Q. Zhang, B.-Q. Li, J.-Q. Huang, *J. Energy Chem.* **2022**, *66*, 24–29.

[16] R. Yan, Z. Zhao, M. Cheng, Z. Yang, C. Cheng, X. Liu, B. Yin, S. Li, *Angew. Chem. Int. Ed.* **2023**, *62*, e202215414.
[17] B. Chen, T. Wang, S. Zhao, J. Tan, N. Zhao, S. P. Jiang, Q. Zhang, G. Zhou, H.-M. Cheng, *Adv. Mater.* **2021**, *33*, 2007090.
[18] Y. Li, Y. Ji, Y. Zhao, J. Chen, S. Zheng, X. Sang, B. Yang, Z. Li, L. Lei, Z. Wen, X. Feng, Y. Hou, *Adv. Mater.* **2022**, *34*, 2202240.
[19] L. Wang, W. Hua, X. Wan, Z. Feng, Z. Hu, H. Li, J. Niu, L. Wang, A. Wang, J. Liu, X. Lang, G. Wang, W. Li, Q.-H. Yang, W. Wang, *Adv. Mater.* **2022**, *34*, 2110279.
[20] Y.-Q. Peng, M. Zhao, Z.-X. Chen, Q. Cheng, Y. Liu, C.-X. Zhao, X. Ma, B.-Q. Li, C.-M. Chen, J.-Q. Huang, Q. Zhang, *Batteries Supercaps* **2022**, *5*, e202100359.
[21] Y. Qiao, K. Jiang, H. Deng, H. Zhou, *Nat. Catal.* **2019**, *2*, 1035–1044.
[22] C. Ye, J. Shan, D. Chao, P. Liang, Y. Jiao, J. Hao, Q. Gu, K. Davey, H. Wang, S.-Z. Qiao, *J. Am. Chem. Soc.* **2021**, *143*, 16902–16907.
[23] Y. Yan, C. Cheng, L. Zhang, Y. Li, J. Lu, *Adv. Energy Mater.* **2019**, *9*, 1900148.
[24] Q. Gu, J. A. Kimpton, H. E. Brand, Z. Wang, S. Chou, *Adv. Energy Mater.* **2017**, *7*, 1602831.
[25] S. Li, Z. Zeng, J. Yang, Z. Han, W. Hu, L. Wang, J. Ma, B. Shan, J. Xie, *ACS Appl. Energy Mater.* **2019**, *2*, 2956–2964.
[26] A. Kumar, A. Ghosh, M. Forsyth, D. R. MacFarlane, S. Mitra, *ACS Energy Lett.* **2020**, *5*, 2112–2121.
[27] X. Xu, D. Zhou, X. Qin, K. Lin, F. Kang, B. Li, D. Shanmukaraj, T. Rojo, M. Armand, G. Wang, *Nat. Commun.* **2018**, *9*, 3870.
[28] J. Xiao, G. Zhou, H. Chen, X. Feng, D. Legut, Y. Fan, T. Wang, Y. Cui, Q. Zhang, *Nano Lett.* **2019**, *19*, 7487–7493.
[29] J. Shan, J. Liao, C. Ye, J. Dong, Y. Zheng, S.-Z. Qiao, *Angew. Chem. Int. Ed.* **2022**, *61*, e202213412.
[30] X. Yang, X. Gao, Q. Sun, S. P. Jand, Y. Yu, Y. Zhao, X. Li, K. Adair, L.-Y. Kuo, J. Rohrer, J. Liang, X. Lin, M. N. Banis, Y. Hu, H. Zhang, X. Li, R. Li, H. Zhang, P. Kaghazchi, T.-K. Sham, X. Sun, *Adv. Mater.* **2019**, *31*, 1901220.
[31] G. Tan, R. Xu, Z. Xing, Y. Yuan, J. Lu, J. Wen, C. Liu, L. Ma, C. Zhan, Q. Liu, T. Wu, Z. Jian, R. Shahbazian-Yassar, Y. Ren, D. J. Miller, L. A. Curtiss, X. Ji, K. Amine, *Nat. Energy* **2017**, *2*, 17090.
[32] Q. He, A. T. S. Freiberg, M. U. M. Patel, S. Qian, H. A. Gasteiger, *J. Electrochem. Soc.* **2020**, *167*, 080508.
[33] I. A. Pankin, A. Martini, K. A. Lomachenko, A. V. Soldatov, S. Bordiga, E. Borfecchia, *Catal. Today* **2020**, *345*, 125–135.
[34] H. Funke, A. C. Scheinost, M. Chukalina, *Phys. Rev. B* **2005**, *71*, 094110.
[35] J. Timoshenko, A. Kuzmin, *Comput. Phys. Commun.* **2009**, *180*, 920–925.
[36] G. Zhou, S. Zhao, T. Wang, S.-Z. Yang, B. Johannessen, H. Chen, C. Liu, Y. Ye, Y. Wu, Y. Peng, C. Liu, S. P. Jiang, Q. Zhang, Y. Cui, *Nano Lett.* **2020**, *20*, 1252–1261.
[37] Y. Tu, H. Li, D. Deng, J. Xiao, X. Cui, D. Ding, M. Chen, X. Bao, *Nano Energy* **2016**, *30*, 877–884.

Manuscript received: February 2, 2023
Accepted manuscript online: March 28, 2023
Version of record online: April 20, 2023